Extracted from

International Masonry Conference 2026

State of the Art in Masonry Research

Proceedings of the
11th International Masonry Conference (IMC 2026), Lübeck, Germany,
12–15 July 2026

Edited by Birger Gigla, Miklós Molnár and Nigel Shrive

Published by
The International Masonry Society
c/o Lucideon Limited – Stone Business Park, Brooms Road, Stone, Staffs, ST15 0SH

Link to the full conference proceedings

Fraunhofer IRB Verlag

Full-field identification of elastic and shear moduli of perforated masonry walls using DIC and stiffness-based shear partition (Euler-Bernoulli vs Timoshenko)

Comparison across clay brick, calcium silicate brick, and calcium silicate block masonry

Navid Vafa, Paul A. Korswagen, Jan G. Rots

Abstract: Digital Image Correlation (DIC) is increasingly used in masonry testing for full-field crack mapping, yet its potential for quantitative identification of elastic properties at structural scale is still not fully exploited for perforated walls where load paths split into multiple piers. This contribution presents a DIC-driven procedure to estimate the Young's modulus E and the shear modulus G of windowed masonry walls made of three materials: clay brick masonry, calcium silicate brick masonry, and calcium silicate block masonry. Axial strains are extracted at the wall extreme fibres and converted to E using section-dependent bending stresses that account for the reduced cross-section within the window height. For G, pier-average shear strains are obtained from DIC strain fields within defined regions of interest, while pier shear forces are computed by stiffness-based partition of the applied top shear between the left and right piers. Two bounds are considered: Euler–Bernoulli theory (shear-rigid) and Timoshenko theory (shear-flexible) with a shear correction factor. The comparison clarifies how the inferred G depends on pier aspect ratio and the assumed shear deformability. Finally, a parametric study is conducted to quantify how the assumed Poisson's ratio affects the back-calculation of E from the measured G. The results further indicate that elastic parameters obtained from standard small-scale tests (e.g., prisms or wallets) tend to overestimate the effective E and G inferred at wall scale, which can significantly bias the calibration of continuum and macro-element numerical models.

Keywords: Digital Image Correlation; masonry walls; elastic modulus; shear modulus; Timoshenko; perforated walls

https://doi.org/10.60628/9783738810400-1017

1 Introduction

Mechanical characterization of masonry at structural scale is non-trivial because the measured stiffness depends on boundary conditions, specimen geometry, and the progressive localization of cracking. This is particularly relevant for perforated walls with openings, where the load path is forced through multiple piers and the applied top shear is not shared uniformly. In practice, wall stiffness inferred from global force–displacement curves mixes flexure, shear, rocking and local slip, and therefore it is difficult to associate a single modulus with the observed response.

Digital Image Correlation (DIC) provides full-field displacement and strain maps and has matured into a robust measurement method for structural tests when camera calibration, speckle quality and correlation settings are properly controlled [1–3]. For masonry walls tested in-plane, DIC has been used to interpret deformation modes and strain localization more reliably than sparse gauge layouts [4]. Beyond qualitative interpretation, full-field data also enables property identification by linking measured strains to internally consistent stress estimates.

A key obstacle for estimating shear modulus in perforated walls is the distribution of shear force between piers. If the left and right piers have different widths, their flexural and shear stiffnesses differ; the top shear will therefore be partitioned according to stiffness rather than geometry alone. In this paper, the partition is computed using two classical beam idealizations: Euler–Bernoulli theory, which neglects shear deformation, and Timoshenko theory, which includes it through a shear correction factor [5,6]. Comparing both provides a transparent sensitivity bound that is particularly informative for stocky piers where shear deformation is expected to contribute to lateral compliance. The objective is to present a consistent workflow to estimate the Young's modulus E, shear modulus G for three masonry typologies (clay brick, calcium silicate brick, and calcium silicate block) tested as windowed walls under quasi-static in-plane lateral loading with cantilever boundary conditions.

2 Experimental program

2.1 Specimens

The study considers five perforated wall typologies with comparable global geometry and one window opening: one clay brick masonry (CLBR), two calcium silicate brick masonry (CSBR), and two calcium silicate block masonry (CSBL). For each wall, the overall height H, length L, thickness T, opening length Lw, and the pier widths (left bL, right bR) are measured and recorded to support stress calculations as shown in Figure 1. The thickness of all the samples is 100 mm.

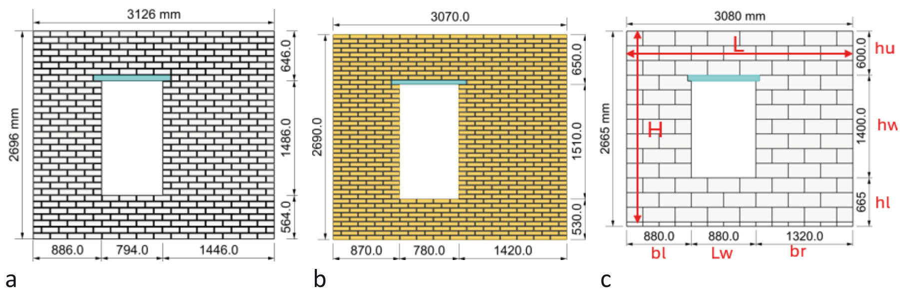

Fig. 1 Samples geometry and material: a- CSBR, b- CLBR, c- CSBL.

2.2 Boundary conditions and loading protocol

Walls are tested under quasi-static monotonic (pushover) in-plane loading. The base is fully fixed, while the top boundary is free to rotate, promoting a cantilever-like global response. Images for DIC are acquired at predefined displacement intervals, resulting in synchronized stages that include photo index, applied force F, and actuator displacement Ux at the top as shown in Figure 2.

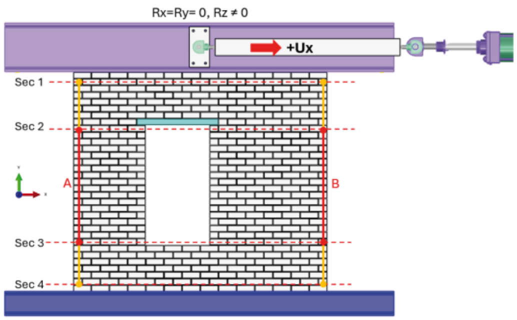

Fig. 2 Boundary conditions, and the location of tensile (A) and compressive (B) Extensometers.

2.3 DIC setup

A high-contrast speckle pattern was specifically designed and applied to each wall to enable reliable detection of crack openings down to approximately 0.1 mm (Fig. 3). The DIC correlation was performed using a subset size of 40 pixels and a point spacing (step size) of 20 pixels. Two-dimensional measurements were acquired using a Canon EOS 5DS camera (51 MP). To ensure uniform, shadow-free illumination and maximize image contrast throughout the test, a studio strobe flash was positioned approximately perpendicular to the wall surface. The 2D DIC analyses were carried out in GOM Correlate software [7]. Two displacement measures are used: Ux from the actuator and U_DIC from the DIC tracking of the last row of the wall.

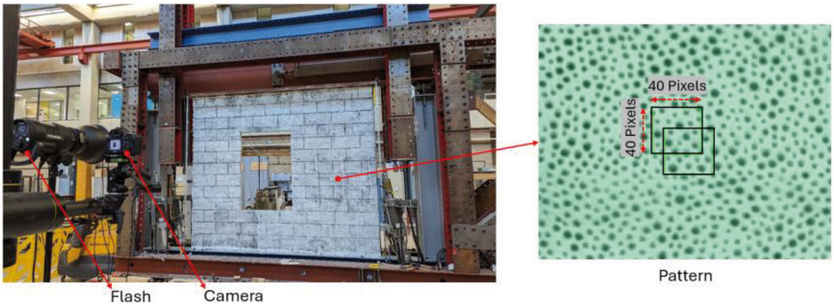

Fig. 3 DIC setup: camera location and applied pattern.

3 DIC-based identification methodology

3.1 Section-dependent bending stresses for perforated walls

To convert DIC axial strains to Young's modulus, bending stresses are evaluated using classical beam theory, while accounting for the reduction of cross-section within the window height. Four cross-sections are defined along the wall height (Fig. 2). Sections 1 and 4 lie outside the opening zone and use the full rectangular section (width L, thickness T). Sections 2 and 3 lie within the window height and use a composite "piers-only" section consisting of two rectangles (bl×T and br×T) separated by the opening length.

$$\sigma(x) = \sigma_0 + \frac{M}{I}\,(x - x_{\mathrm{NA}}) \qquad (1)$$

In Eq. (1), x is the horizontal coordinate across the wall, x_NA is the neutral axis position, I(z) is the second moment of area of the relevant section, and σ0 is a constant axial stress of 0.12 MPa due to the top steel beam. The bending moment is obtained from the measured lateral force and the lever arm to the considered section.

$$M_i^{(j)} = V^{(j)}\,H_i \qquad (2)$$

Because the moment varies approximately linearly with height for the cantilever-like configuration, a zone-average stress is computed based on Eq.(3) between the bounding sections of 1-4 and 2-3 in Figure 2.

$$\bar{\sigma}_{A,14}^{(j)} = \frac{\sigma_{A,S1}^{(j)}+\sigma_{A,S4}^{(j)}}{2},\ \bar{\sigma}_{B,14}^{(j)} = \frac{\sigma_{B,S1}^{(j)}+\sigma_{B,S4}^{(j)}}{2} \qquad (3)$$

$$\bar{\sigma}_{A,23}^{(j)} = \frac{\sigma_{A,S2}^{(j)}+\sigma_{A,S3}^{(j)}}{2},\ \bar{\sigma}_{B,23}^{(j)} = \frac{\sigma_{B,S2}^{(j)}+\sigma_{B,S3}^{(j)}}{2}$$

3.2 Young's modulus from extreme-fibers axial strains

To obtain a single representative elastic modulus for each wall, only the pre-cracking response is considered; in this study, this corresponds to 10–40% of the peak force. The axial strain distribution between Sections 1 and 4 is extracted from the DIC fields by defining virtual extensometers: a long gauge spanning the full wall height and shorter gauges placed locally to capture the deformation of the individual piers, as illustrated in Fig. 2. At each load stage i, an instantaneous modulus estimate is computed as:

$$E_{A,14}^{(j)} = \frac{|\bar{\sigma}_{A,14}^{(j)}|}{|\varepsilon_{A,14}^{(j)}|}, E_{B,14}^{(j)} = \frac{|\bar{\sigma}_{B,14}^{(j)}|}{|\varepsilon_{B,14}^{(j)}|} \qquad (4)$$

$$E_{A,23}^{(j)} = \frac{|\bar{\sigma}_{A,23}^{(j)}|}{|\varepsilon_{A,23}^{(j)}|}, E_{B,23}^{(j)} = \frac{|\bar{\sigma}_{B,23}^{(j)}|}{|\varepsilon_{B,23}^{(j)}|}$$

3.3 Shear-force partition between piers

To obtain shear modulus from DIC, we need the pier shear force V_1(left pier) and V_2(right pier), such that:

$$V_1 + V_2 = V \qquad (5)$$

A practical solution is a stiffness-based partition in which each pier attracts a share of the applied shear proportional to its lateral stiffness. Selecting an appropriate classical formulation, however, is not straightforward because the effective stiffness depends on the specimen geometry (e.g., pier width, aspect ratio, and opening configuration) and therefore varies from one wall to another. Let each pier $i \in \{1,2\}$have width b_i(equal to $b_L$or b_R), thickness T, and effective height h_p. We can define sectional properties as:

$$A_i = b_i T, I_i = \frac{T b_i^3}{12} \qquad (6)$$

3.3.1 Euler–Bernoulli (shear-rigid) pier stiffness

For a cantilever beam of height h_p, tip shear–deflection relation under Euler–Bernoulli bending is:

$$\delta_{b,i} = \frac{V_i h_p^3}{3EI_i} \Rightarrow k_{EB,i} = \frac{V_i}{\delta_{b,i}} = \frac{3EI_i}{h_p^3} \qquad (7)$$

Hence the shear partition becomes:

$$V_{1,EB} = V \frac{k_{EB,1}}{k_{EB,1} + k_{EB,2}}, V_{2,EB} = V \frac{k_{EB,2}}{k_{EB,1} + k_{EB,2}} \qquad (8)$$

This predicts stronger attraction of shear to the stiffer pier through $I_i \propto b_i^3$, which can be significant when one pier is notably narrower.

3.3.2 Timoshenko (shear-flexible) pier stiffness

Timoshenko adds shear deflection:

$$\delta_{s,i} = \frac{V_i h_p}{\kappa G A_i} \qquad (9)$$

so total lateral deflection is:

$$\delta_{T,i} = \delta_{b,i} + \delta_{s,i} = \frac{V_i h_p^3}{3EI_i} + \frac{V_i h_p}{\kappa G A_i} \qquad (10)$$

Therefore the effective stiffness is:

$$k_{T,i} = (\frac{h_p^3}{3EI_i} + \frac{h_p}{\kappa G A_i})^{-1} \qquad (11)$$

and partition becomes:

$$V_{1,T} = V \frac{k_{T,1}}{k_{T,1} + k_{T,2}}, V_{2,T} = V \frac{k_{T,2}}{k_{T,1} + k_{T,2}} \qquad (12)$$

The key difference is that when h_p/b_i is small (a "stockier" pier), shear deformation can be non-negligible, making Timoshenko more realistic; when h_p/b_i is larger (a slender pier), Euler–Bernoulli may already be close. The shear correction factor κ can be taken as $\kappa \approx 5/6$ for rectangular section [5].

3.4 Shear modulus from DIC shear strain

Within each pier, DIC provides displacement fields $u(x, y)$ and $v(x, y)$. Shear strain is evaluated as:

$$\gamma_{xy} = \frac{\partial u}{\partial y} + \frac{\partial v}{\partial x} \qquad (13)$$

A pier-average shear strain $\bar{\gamma}_i^{(j)}$ is obtained over a selected ROI. Pier-average shear stress is estimated from the partitioned shear:

$$\bar{\tau}_i^{(j)} = \frac{V_i^{(j)}}{A_i} = \frac{V_i^{(j)}}{b_i T} \qquad (14)$$

Therefore, the shear modulus follows:

$$G_i^{(j)} = \frac{|\bar{\tau}_i^{(j)}|}{|\bar{\gamma}_i^{(j)}|} \qquad (15)$$

Furthermore, by assuming an effective isotropic elastic relation at the scale of interest:

$$E \approx 2G(1 + \nu) \qquad (16)$$

Using Eq. (16), the Young's modulus can be obtained directly; however, the result is highly sensitive to the assumed value of Poisson's ratio.

4 Results and discussion

4.1 Global force–displacement response

Figure 4 compares the force–displacement response based on the actuator-imposed displacement with the displacement measured by DIC. The close agreement between the two curves confirms proper synchronization and alignment of the data streams and supports the reliability of the DIC-derived displacement measurements used in the subsequent analyses.

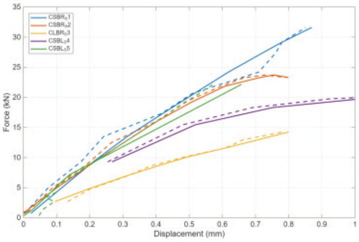

Fig. 4 Global force–displacement curves using actuator displacement and DIC-derived displacement.

4.2 Identified Young's modulus in tension and compression

These boxplots are presenting the elastic moduli (median over 10–40% of peak force) grouped by material. As can be seen, these values are much lower than what normally will be obtained from a compressive test on a prism or wallet.

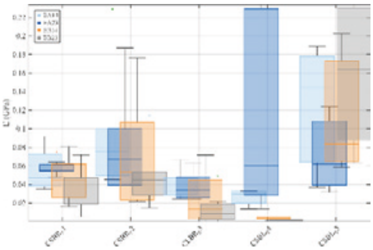

Fig. 5 Elastic modulus obtained from compressive and tensile fibers.

4.3 Shear partition sensitivity and its effect on G

The Euler–Bernoulli partition generally allocates a larger fraction of shear to the wider (stiffer) pier because k_EB scales strongly with I. When piers are stocky, Timoshenko partition moderates this effect due to the additional shear compliance term as shown in Figure 6. This directly influences $\bar{\tau}$ and therefore the inferred G.

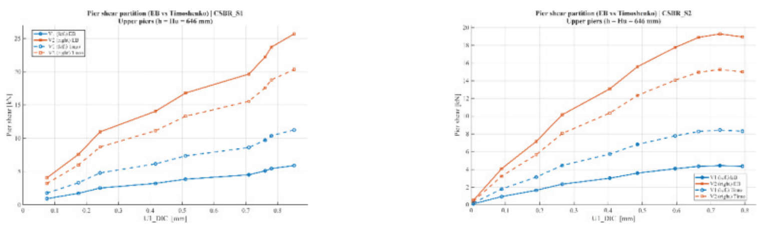

a- CSBR_S1

b- CSBR-S2

Fig. 6 Comparison between shear force from Euler-Bernoulli vs Timoshenko on piers.

4.4 Shear modulus G

To determine the shear modulus, the pier shear strain must first be evaluated. From the DIC displacement fields, the lateral deformation of each pier is tracked at every imposed displacement step, as illustrated in Fig. 7. By computing the relative lateral displacement between the top and bottom of the window zone, the corresponding shear strain is obtained according to Eq. (13). Combining this shear strain with the pier shear force (Eq. (15)) allows the shear modulus to be calculated. Figure 8 presents the resulting shear modulus for the left and right piers, highlighting the influence of the assumed shear-force distribution based on Euler–Bernoulli and Timoshenko formulations.

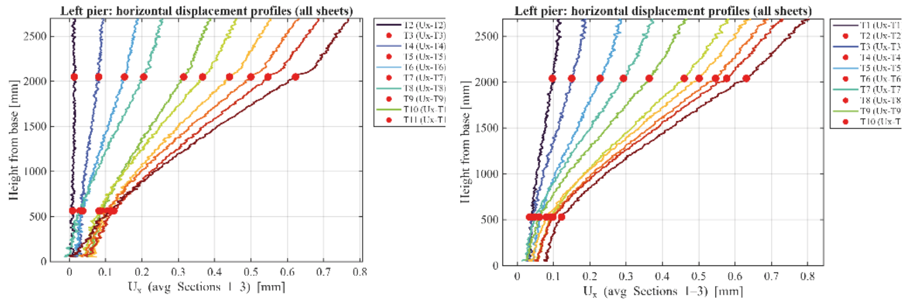

a- CSBR-S2 b- CLBR-S3

Fig. 7 Tracking the lateral deformation of piers during monotonic loading.

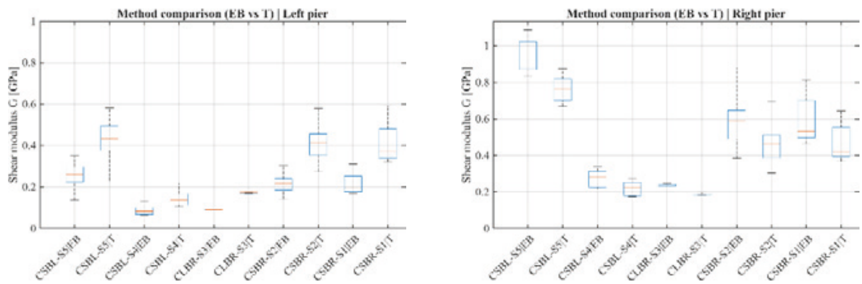

a- Left piers b- Right piers

Fig. 8 Comparison of shear modulus on the left and right piers.

4.5 Elastic modulus derived from G

With the shear modulus identified and assuming the wall response remains within the elastic regime (i.e., prior to crack initiation), the Young's modulus can also be back-calculated using Eq. (16). Although this estimate depends on Poisson's ratio, the expected range for masonry ($\nu \approx 0.10$–0.20) enables a practical sensitivity study to quantify its influence. In this work, the effect is illustrated for the left pier, where the comparison between Euler–Bernoulli and Timoshenko shear-force partitions shows that the Timoshenko-based approach consistently yields a higher back-calculated Young's modulus.

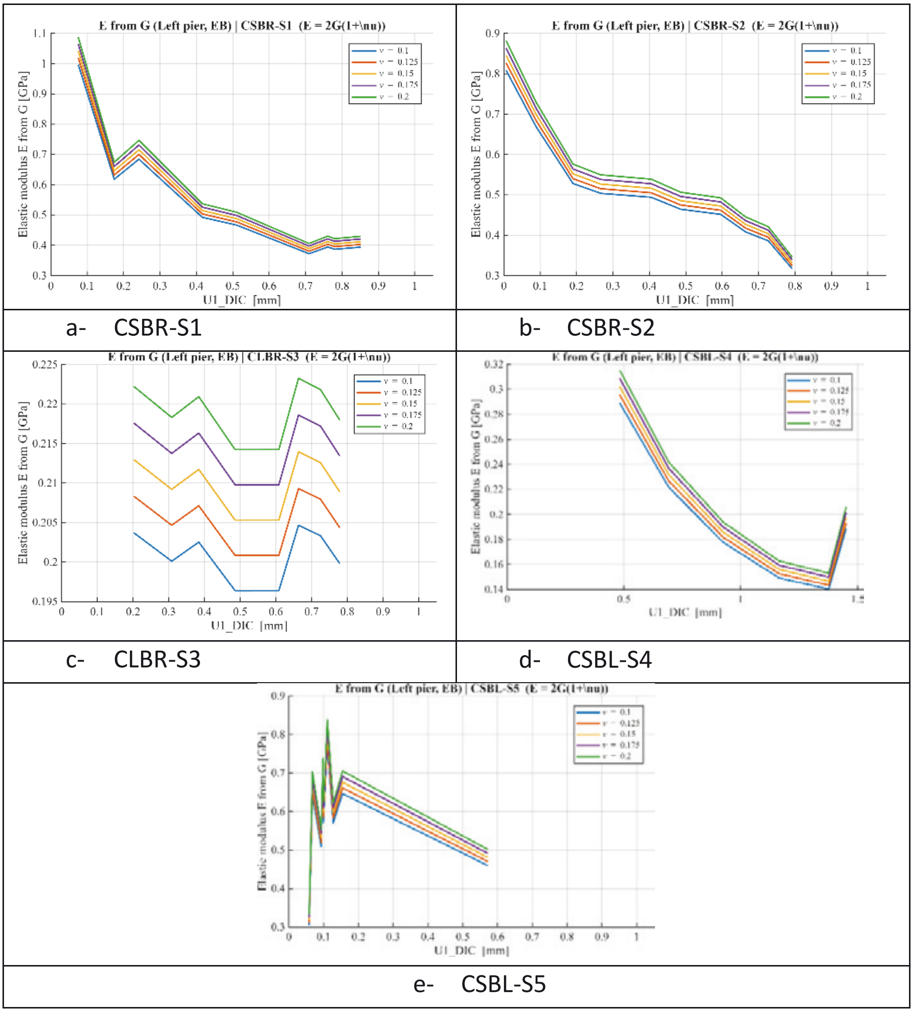

Fig. 9 Elastic modulus and the influence of Poisson's ratio.

5 Conclusions

A DIC-driven workflow was developed to identify the Young's modulus E and shear modulus G of perforated masonry walls under in-plane lateral loading. Section-dependent bending stresses, accounting for the opening, enabled conversion of extreme-fiber axial strains into representative pre-cracking values of E in tension and compression.

For G, pier shear strains from DIC were combined with a stiffness-based partition of the applied shear between piers. Comparing Euler–Bernoulli and Timoshenko formulations showed that the assumed shear-force distribution can significantly influence the identified moduli; Timoshenko-based partition generally led to higher inferred stiffness, especially for stocky piers where shear deformation is more relevant. A clear discrepancy was also observed between E obtained from axial extreme-fiber strains and E back-calculated from shear deformation, while Poisson's ratio proved critical in the E–G conversion and should be treated through a sensitivity study within the typical masonry range.

Finally, wall-scale moduli from full-field measurements were consistently lower than values from standard small-scale tests (prisms/wallets), implying that using small-specimen properties may overestimate linear stiffness in continuum or macro-element models and bias structural assessments.

6 References

[1] Hild, François, and Stéphane Roux. "Digital image correlation: from displacement measurement to identification of elastic properties–a review." Strain 42, no. 2 (2006): 69-80.

[2] Schreier, H., Orteu, J.-J., Sutton, M.A.: Image Correlation for Shape, Motion and Deformation Measurements: Basic Concepts, Theory and Applications. Springer.

[3] Howlader, M. K., M. J. Masia, and M. C. Griffith. "Digital image correlation for the analysis of in-plane tested unreinforced masonry walls." In *Structures*, vol. 29, pp. 427-445. Elsevier, 2021.

[4] Cowper, GR0151. "The shear coefficient in Timoshenko's beam theory." (1966): 335-340.

[5] Dong, Stanley B., Can Alpdogan, and Ertugrul Taciroglu. "Much ado about shear correction factors in Timoshenko beam theory." International Journal of Solids and Structures 47, no. 13 (2010): 1651-1665.

[6] GOM GmbH. (2026). https://www.gom.com